NANO LETTERS

Letter

pubs.acs.org/NanoLett

The Interplay between Trap Density and Hysteresis in Planar Heterojunction Perovskite Solar Cells

Jin-Wook Lee,[†] Seul-Gi Kim,[‡] Sang-Hoon Bae,[†] Do-Kyoung Lee,[‡] Oliver Lin,[†] Yang Yang,*[,†] and Nam-Gyu Park*[,‡]

[†]Department of Materials Science and Engineering and California NanoSystems Institute, University of California, Los Angeles, California 90095, United States

[‡]School of Chemical Engineering, Sungkyunkwan University (SKKU), Suwon 440-746, Korea

Supporting Information

ABSTRACT: Anomalous current−voltage (J−V) hysteresis in perovskite (PSK) solar cell is open to dispute, where hysteresis is argued to be due to electrode polarization, dipolar polarization, and/or native defects. However, a correlation between those factors and J−V hysteresis is hard to be directly evaluated because they usually coexist and are significantly varied depending on morphology and crystallinity of the PSK layer, selective contacts, and device architecture. In this study, without changing morphology and crystallinity of PSK layer in a planar heterojunction structure employing $FA_{0.9}Cs_{0.1}PbI_3$, a correlation between J−V hysteresis and trap density is directly evaluated by means of thermally induced PbI_2 regulating trap density. Increase in thermal annealing time at a given temperature of 150 °C induces growth of PbI_2 on the PSK grain surface, which results in significant reduction of nonradiative recombination. Hysteresis index is reduced from 0.384 to 0.146 as the annealing time is increased from 5 to 100 min due to decrease in the amplitude of trap-mediated recombination. Reduction of hysteresis by minimizing trap density via controlling thermal annealing time leads to the stabilized PCE of 18.84% from the normal planar structured $FA_{0.9}Cs_{0.1}PbI_3$ PSK solar cell.

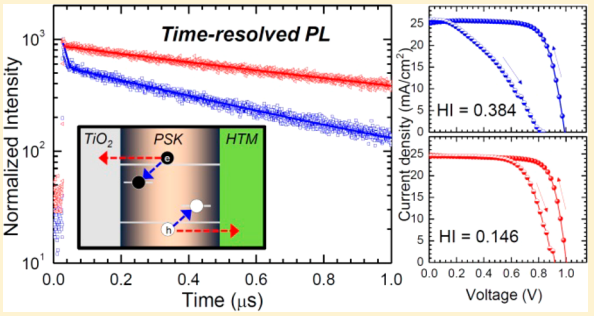

KEYWORDS: *Perovskite, solar cell, hysteresis, defect, passivation, trap density*

Exploration of photovoltaic materials discovered perovskite (PSK) photovoltaics thanks to the pioneering works on PSK-sensitized solar cells in 2009[1] and 2011[2] and the breakthrough reports on solid-state PSK solar cells in 2012.[3,4] The first report[3] on a long-term stable solid-state PSK solar cell incorporating a solid hole transporting material triggered tremendous follow-up researches. As of March 13, 2017, a state-of-the-art technology achieved a certified power conversion efficiency (PCE) of 22.1%,[5] which can be attributed to the development of specialized coating techniques and optimization of PSK composition.[6−11]

In the meantime, with impressive evolution of device performance a surge of research efforts have been devoted to investigate the fundamentals of PSK materials. The superb photovoltaic performance of the PSK solar cells was attributed to beneficial optoelectronic properties such as high absorption coefficient,[7] long-range balanced charge carrier lifetime,[12−14] defect tolerance,[15] and low exciton binding energy.[16] On the other hand, several anomalous phenomena have been observed such as ferroelectric behavior,[17] ion migration,[18] and dynamic motion of organic cations,[19,20] which was associated with current−voltage (J−V) hysteresis in devices.[21,22] PSK solar cells require accurate measurement because of large dependency of J−V characteristics on scan direction and rate.[21,22] Now, as an alternative way, the stabilized power output under continuous light and bias voltage corresponding to the maximum power point is accepted as a standard procedure although the origin of the J−V hysteresis has not been fully understood.

The J−V hysteresis is related to capacitive current in the full devices.[23] The origin of the capacitive current has been studied using a variety of techniques,[19,22−27] from which several possible factors have been drawn: (i) electrode polarization due to accumulation of charged spices at interfaces,[23−25] (ii) dipolar polarization of microscopic (ferroelectric) domains associated with molecular orientation,[26] and (iii) native defects in PSK layer.[17,27] However, such factors usually coexist and are significantly varied depending on morphology and crystallinity of the PSK layer, selective contacts, and device architecture. As a result, it is difficult to find a direct correlation between those factors and J−V hysteresis. Therefore, we were motivated to investigate the correlation between the factors and J−V hysteresis.

In this study, we elaborate a correlation between defects in $FA_{0.9}Cs_{0.1}PbI_3$ layer and J−V hysteresis in PSK solar cell by means of thermally induced PbI_2, where PbI_2 is thermally

Received: March 22, 2017
Revised: June 2, 2017
Published: June 6, 2017

DOI: 10.1021/acs.nanolett.7b01211
Nano Lett. XXXX, XXX, XXX−XXX

grown on the surface of PSK grains by controlling annealing time. Effects of annealing time on crystallinity and morphology of PSK were investigated by scanning electron microscopy (SEM) and X-ray diffraction (XRD) measurements. Correlation between the thermally induced PbI_2 and defect density was investigated by time-resolved photoluminescence (TRPL) measurement, which was discussed in conjunction with $J-V$ hysteresis in planar PSK solar cells employing $FA_{0.9}Cs_{0.1}PbI_3$. Finally, with optimized thermal annealing time a stabilized PCE of 18.84% was demonstrated.

The $FA_{0.9}Cs_{0.1}PbI_3$ PSK layer was formed by an adduct approach as described previously,[28] in which the heat-treatment (annealing) time at 150 °C was varied from 5 to 100 min (Figure 1a). Absorption spectra of the $FA_{0.9}Cs_{0.1}PbI_3$ films as a function of the annealing time are shown in Figure 1b. Absorbance in the ranging between about 550 and 780 nm is decreased as annealing time is increased (it is clearly seen from the change in absorbance at 600 nm with annealing time in the inset of Figure 1b), which indicates $FA_{0.9}Cs_{0.1}PbI_3$ is likely to be partially decomposed upon prolonged annealing at 150 °C.

To check the decomposition of the PSK layer, XRD patterns were recorded with different annealing time (Figure 2a). XRD peaks are indexed to pure black phase of $FAPbI_3$ without the presence of the yellow phase.[7,8] Notably, as the annealing time is increased the peak at around 12.6° originated from (001) plane of PbI_2 (indicated by *) appears and its intensity is

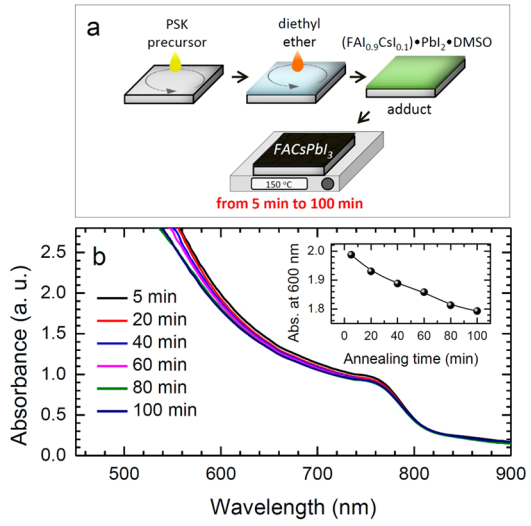

Figure 1. (a) Experimental procedure for formation of $FA_{0.9}Cs_{0.1}PbI_3$ PSK layer via adduct intermediate. (b) Absorption spectra of $FA_{0.9}Cs_{0.1}PbI_3$ PSK films as a function of annealing time at 150 °C. The perovskite films were spin-coated on glass substrate and annealed at 65 °C for 1 min and 150 °C for a varied time ranging from 5 to 100 min. Inset shows change in absorbance at 600 nm with annealing time.

gradually increased, which is indicative of partial decomposition of $FA_{0.9}Cs_{0.1}PbI_3$. The ratio of (001) peak intensity of PbI_2 to (101) peak intensity of PSK is exponentially increased from 0.03, 0.04, 0.07, 0.10, 0.14, and 0.23 as the annealing time is increased from 5, 20, 40, 60, 80, and 100 min, respectively. Furthermore, it is noted that full width at half-maximum (fwhm) for the (101) PSK peak is hardly changed (0.073 ± 0.01 °) with prolonged annealing time (Figure 2b), which implies that the crystallite size of the film is not affected by annealing time.[29]

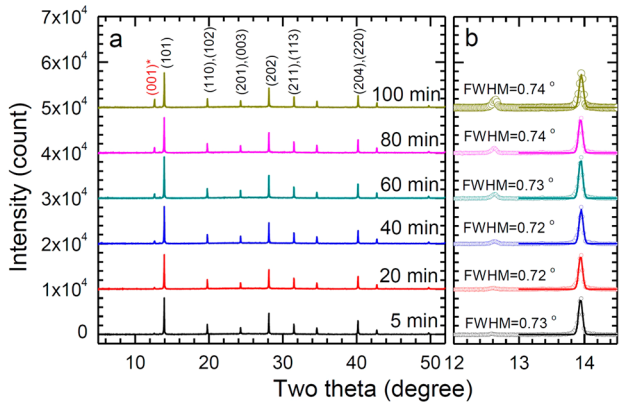

Figure 2. (a) X-ray diffraction (XRD) patterns of $FA_{0.9}Cs_{0.1}PbI_3$ PSK film as a function of annealing time at 150 °C. The PSK films were spin-coated on a glass substrate and annealed at 65 °C for 1 min and 150 °C for a varied time ranging from 5 to 100 min. All the peaks are indexed to black phase of $FA_{0.9}Cs_{0.1}PbI_3$, whereas the peak indicated by * is indexed to (001) plane of PbI_2. (b) The XRD spectra in low angle region, showing (001) peak for PbI_2 and (101) peak for $FA_{0.9}Cs_{0.1}PbI_3$. Open circles represent the measured data and solid lines indicate the fitted data with Gaussian function.

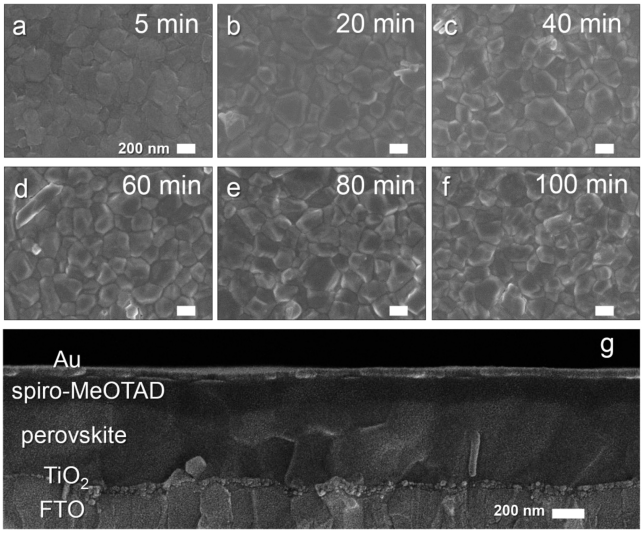

Figure 3. (a–f) Plane-view scanning electron microscopic (SEM) images of $FA_{0.9}Cs_{0.1}PbI_3$ PSK films as a function of annealing time at 150 °C. The perovskite films were spin-coated on a compact TiO_2-coated FTO glass and annealed at 65 °C for 1 min and 150 °C for a varied time ranging from 5 to 100 min. (g) Cross-sectional SEM image of a planar heterojunction solar cell based on $FA_{0.9}Cs_{0.1}PbI_3$ annealed for 40 min at 150 °C.

Change in morphology of the PSK films with different annealing time is investigated from the plane-view SEM images in Figure 3a–f, where morphology is hardly changed with annealing time. No significant change in grain size is consistent with X-ray crystallite sizes with almost identical fwhm's observed in Figure 2b. All the films show similar morphology with grain size of about 200–300 nm. However, a closer inspection of the plane-view SEM images reveals that the relative brightness of the grain boundaries compared to grain interiors, is enhanced with prolonged annealing time, which is probably related to the thermally induced PbI_2 because the decomposition is assumed to occur from grain boundaries.[30] We fabricated planar heterojunction PSK solar cells with a

DOI: 10.1021/acs.nanolett.7b01211
Nano Lett. XXXX, XXX, XXX–XXX

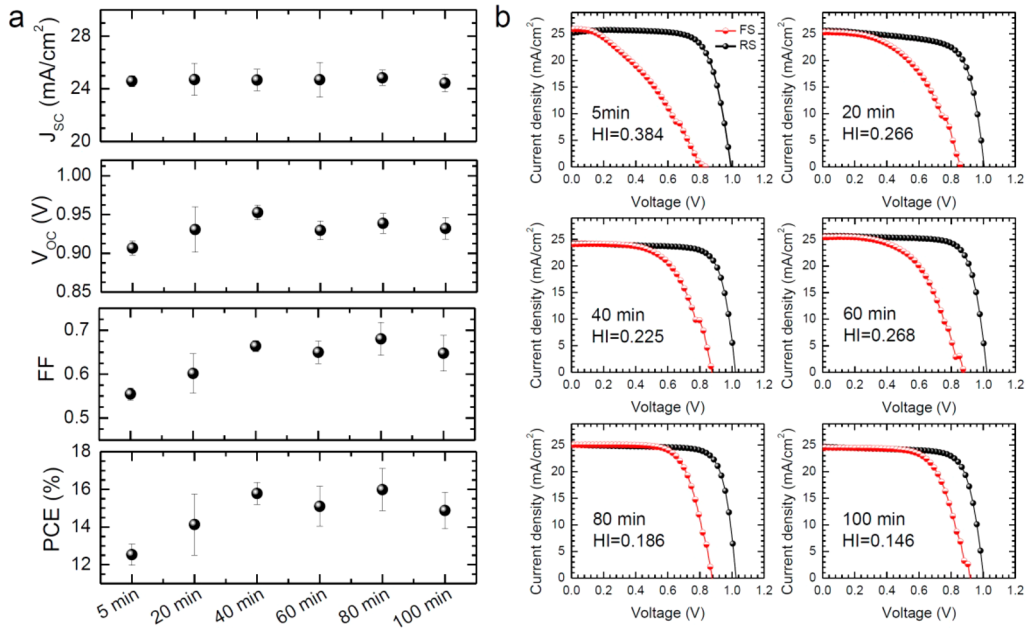

Figure 4. (a) Dependence of photovoltaic parameters of J_{SC}, V_{OC}, FF, and PCE of $FA_{0.9}Cs_{0.1}PbI_3$ PSK solar cells on annealing time at 150 °C. All the parameters represent the arithmetic mean of the FS data and the RS data measured at scan rate of 0.12 V/s. (b) FS and RS J–V curves depending on annealing time and calculated HI.

Table 1. Fitted Parameters Obtained from Time-Resolved Photoluminescence Spectra of $FA_{0.9}Cs_{0.1}PbI_3$ Perovskite Film as a Function of Annealing Time at 150 °C[a]

	5 min	20 min	40 min	60 min	80 min	100 min
A_1	824.1 (60.4%)	391.8 (39.6%)	16.3 (2.18%)			
τ_1 (ns)	6.0	5.2	6.0			
A_2	541.0 (39.6%)	598.4 (60.4%)	730.8 (97.8%)	869.3	859.1	866.6
τ_2 (ns)	575.1	558.2	607.7	719.6	814.6	998.6

[a]The perovskite film was spin-coated on glass substrate and annealed at 65 °C for 1 min and 150 °C for varied time. The data were fit to biexponential decay.

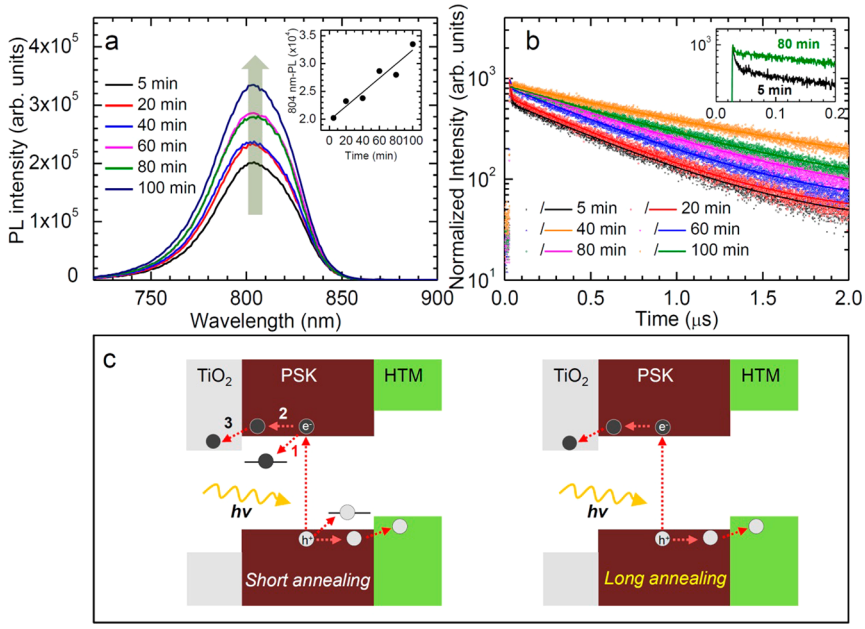

Figure 5. (a) Steady-state and (b) time-resolved PL spectra of $FA_{0.9}Cs_{0.1}PbI_3$ PSK films as a function of annealing time at 150 °C. The PSK films were spin-coated on glass substrate and annealed at 65 °C for 1 min and 150 °C for a varied time ranging from 5 to 100 min. Inset of (a) shows change in intensity of PL peak at 804 nm with annealing time. Open circles in (b) show the measured data while solid lines indicate the fitted data. (c) Charge transport process in PSK solar cell depending on different annealing time.

DOI: 10.1021/acs.nanolett.7b01211
Nano Lett. XXXX, XXX, XXX−XXX

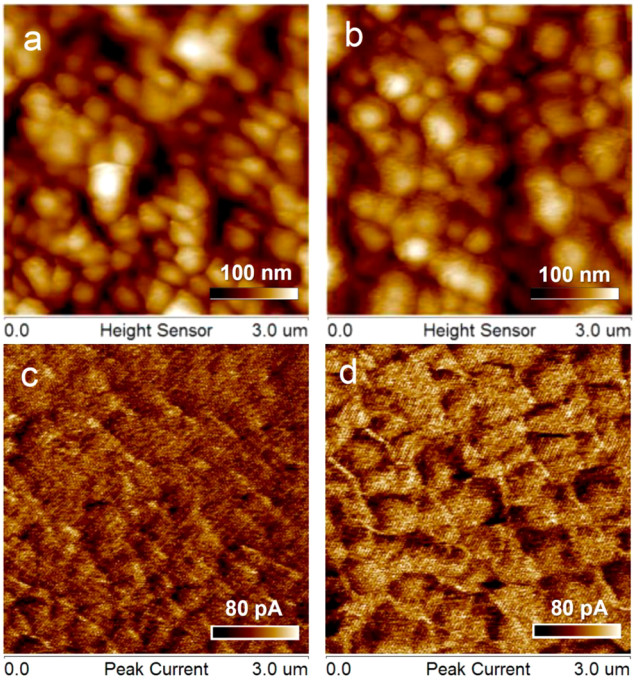

Figure 6. (a,b) Topology and (c,d) conductive atomic force microscopic (c-AFM) images of $FA_{0.9}Cs_{0.1}PbI_3$ films annealed at 150 °C for (a,c) 5 min and (b,d) 80 min. The PSK films were prepared on ITO substrate and the measurement was carried out under room light at bias voltage of 500 mV.

compact TiO_2 film and a spiro-MeOTAD layer as an electron transporting layer and a hole transporting layer, respectively. The cross-sectional SEM image of the device is shown in Figure 3g, in which about 500 nm thick $FA_{0.9}Cs_{0.1}PbI_3$ layer is formed between 60 nm thick compact TiO_2 and 200 nm thick spiro-MeOTAD layers.

Figure 4 shows effect of annealing time on photovoltaic parameters and hysteresis. The parameters in Figure 4a represent the arithmetic mean of the forward (FS, from short-circuit to open circuit) scanned data and the reverse (RS, from open circuit to short-circuit) scanned data measured at scan rate of 0.12 V/s. Additional discussion on scan rate can be found in Supporting Information (Figures S1 and S2 and Tables S1 and S2). Open-circuit voltage (V_{OC}) and fill factor (FF) are drastically increased as the annealing time is increased from 5 to 40 min, while little change in shot-circuit current density (J_{SC}) is observed regardless of the annealing time. By increasing the annealing time from 5 to 40 min, V_{OC} and FF are enhanced from 0.907 ± 0.09 to 0.953 ± 0.09 V (5.1% increment), and 0.555 ± 0.014 to 0.664 ± 0.012 (20% increment), respectively, which results in an improvement of PCE from 12.53 ± 0.56 to 15.1 ± 1.07% (20.5% increment). Further increase in annealing time from 40 min would not improve V_{OC} and FF. Significantly enhanced PCE upon prolonged annealing is mainly due to the decreased current–voltage (J–V) hysteresis as can be seen in Figure 4b. We evaluate the degree of J–V hysteresis by calculating hysteresis index (HI). In this study, the change in J–V hysteresis is pronounced in low bias voltage region (<0.6 V) while the HI defined in the previous studies only reflects the high voltage region (>0.6 V).[19,22] As a result, the calculated HIs according to the previous definition do not follow the trend of ΔPCE (ΔPCE = $[PCE_{FS} - PCE_{RS}]/PCE_{RS}$, PCE_{FS} and PCE_{RS} represent power conversion efficiency measured from forward scan and reverse scan, respectively) as shown in Table S3. Considering that the HI is aimed at quantifying the difference in power output depending on scan direction, HI is newly defined by the eq 1, which reflects the integrated power output with different scan direction

$$\text{Hyteresis Index (HI)} = \frac{\int_{SC}^{OC}(J_{RS}(V) - J_{FS}(V))dV}{\int_{SC}^{OC} J_{RS}(V)dV} \quad (1)$$

In eq 1, $\int_{SC}^{OC} J_{FS}(V)dV$ and $\int_{SC}^{OC} J_{RS}(V)dV$ stand for the area under J–V curves measured from forward and reverse scans, respectively. Higher HI is indicative of more serious hysteresis. The HI is decreased from 0.384 to 0.266 and to 0.225 as the annealing time is increased from 5 to 20 and to 40 min, respectively, leading to enhancement of mean PCE. For the longer annealing time (60, 80, and 100 min), hysteresis is further decreased and thereby 80 min annealing yields the best average PCE of 15.99 ± 1.13% with J_{SC} of 24.83 ± 0.58 mA/cm^2, V_{OC} of 0.938 ± 0.013 V and FF of 0.680 ± 0.037. When considering no distinct change in morphology and crystallinity as confirmed by XRD and SEM, such a significant change in hysteresis might be related to optoelectronic quality of the PSK layer.

Steady-state and time-resolved photoluminescence (PL) measurements are studied to understand any correlation between recombination, associated trap density, and hysteresis (Figure 5). As can be seen in Figure 5a, steady-state PL intensity is gradually increased from 2.02 × 10^4 (5 min) to 3.35 × 10^4 (100 min), while little shift in peak position is observed. This indicates that radiative recombination is enhanced without

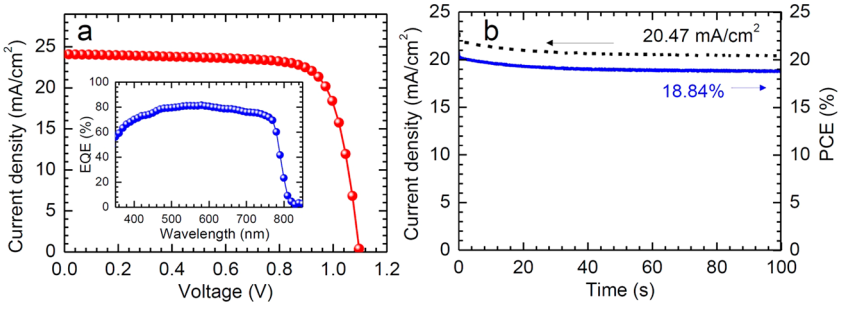

Figure 7. (a) Current density and voltage (J–V) curve and (b) steady-state current density and power conversion efficiency measurement with bias voltage of 0.921 V for the best performing 80 min-annealed $FA_{0.9}Cs_{0.1}PbI_3$ PSK solar cell. Inset of (a) shows external quantum efficiency (EQE) spectrum.

DOI: 10.1021/acs.nanolett.7b01211
Nano Lett. XXXX, XXX, XXX–XXX

changing bandgap. Time-resolved PL is measured in Figure 5b to find the origin of the enhanced steady-state PL intensity in which the films are excited with 640 nm monochromatic beam with a fluence of 0.65 nJ/cm^2. The decay profiles are fitted to either single or biexponential decay function, where the fitted results are listed in Table 1. For the annealing time of 5, 20, and 40 min, the decay profiles show two distinct exponential decay components corresponding to ultrafast ($\tau_1 \sim 5-6$ ns) and much slower decay processes ($\tau_2 > 500$ ns), where the ultrafast decay component (τ_1) is assigned to a trap-mediated nonradiative recombination and the slow one (τ_2) is correlated to radiative recombination.[31−33] It was reported that subgap trap states are saturated if the density of photogenerated charge carriers is much higher than density of the trap-state due to slow detrapping kinetics. In that case, trap-mediated nonradiative recombination would be hindered and bimolecular radiative recombination become dominant.[31,33] As the annealing time is increased from 5 to 20 and to 40 min, the amplitude of τ_1 is decreased from 60.4% to 39.6% to 2.18%. When considering that photogenerated carrier density is the same regardless of annealing time because excitation intensity is not changed, the decrease in τ_1 is indicative of decrease in trap-mediated nonradiative recombination probably due to decrease in defect density by prolonged annealing. For the annealing time longer than 40 min, defect density is further and largely decreased because the ultrafast component disappears mostly. The decay curves are fit to single exponential decay function for the annealing time of 60, 80, and 100 min. Inset of Figure 5b compares the PL decay profiles of the 5 min annealed and 80 min annealed films in which the ultrafast component presented in 5 min sample is clearly eliminated by annealing for 80 min. As listed in Table 1, the τ_2 is significantly increased from 575.1 ns (5 min) to 998.6 ns (100 min), which indicates the lifetime of photogenerated charge carrier in bulk PSK is enhanced.[32] Because the morphology and crystallinity of the PSK films are almost the same regardless of annealing time, the reduced defect density and the enhanced charge carrier lifetime are mainly responsible for the improved performance and $J-V$ hysteresis. In Figure 5c, charge transporting process is schematically presented and compared for short and long annealing time. For short annealing time, the photogenerated charges carriers might be trapped in shallow trap states formed by defects (process 1)[32−34] and thereby the trap-mediated nonradiative recombination occurs. Because of the slow detrapping time, the traps are filled with photogenerated charges under continuous illumination, which is followed by charges collection at the selective contacts (process 2 and 3).[31,33] The trap-filling process might contribute to capacitive current, leading to time-dependent $J-V$ hysteresis, and the loss of charge carriers by nonradiative recombination results in degradation of photovoltaic performance. Defects of PSK film was reported to be passivated by the PbI_2 formed on the surface of PSK grains.[35−40] Structural disorders at grain boundaries were reported to form shallow defect states that potentially trap the charge carriers to induce the nonradiative recombination loss.[41] When considering that thermal decomposition occurs at grain boundaries of the PSK,[30] the prolonged thermal annealing is able to convert the defective PSK grain boundaries to PbI_2 which facilitates the charge carrier separation and reduces the recombination due to advantageous band alignment with the PSK grains.[37,40] However, thermal decomposition of PSK to PbI_2 reduces the film absorbance, as confirmed from absorption spectra in Figure 1. Formation of thick PbI_2 passivation layer was also reported to impede the charge carrier collection,[40] which can be associated with decreased FF for the 100 min annealing. The estimated PbI_2 amount for the 80 min annealing was calculated to be 5.3 mol % from energy dispersive X-ray spectroscopy (EDS) and 3.1 mol % from X-ray photoelectron spectroscopy (XPS). The 5 min annealed film showed less amount of PbI_2 (3.1 mol % from EDS, 0 mol % from XPS) compared to the 80 min annealed film (Figures S3 and S4 and Table S4).

The remaining $J-V$ hysteresis behavior for the prolonged annealing time is assumed to be related to electrode or dipolar polarization.[23−26] A possible origin of electrode polarization is accumulation of charge carriers at the interface between PSK and selective contacts. The accumulation of charge carrier was reported to be associated with mobility of selective contacts affecting charge extraction efficiency from PSK to selective contacts.[24,42] The charge extraction efficiency is assumed to be similar regardless of thermal annealing time in this work because all the devices incorporate same selective contacts. Another possible origin of electrode polarization was suggested to be ion migration, which was found to be dominant through grain boundaries.[43,44] Ferroelectric polarization is also one of responsibilities for hysteresis, which was reported to depend on grain size and composition of PSK layer.[17,26] Because the morphology of the PSK layer is preserved regardless of thermal annealing time, degree of ion migration or ferroelectric polarization in the PSK layer is expected to be similar. Therefore, the observed tendency in HI might be predominantly attributed to change in trap density in the PSK layer.

Conductive atomic force microscopy (c-AFM) is measured to investigate electrical conductivity of the $FA_{0.9}Cs_{0.1}PbI_3$ PSK films formed from different annealing time (Figure 6). Two PSK films, coated on ITO substrate and annealed for 5 and 80 min, are prepared for c-AFM study. Measurements are carried out under room light at bias voltage of 500 mV. In topological images in Figure 6a,b, no significant difference is observed between 5 min annealed sample and 80 min annealed one, which is consistent with SEM images. On the other hand, current is significantly higher for 80 min annealed film than for 5 min annealed one (Figure 6c,d), which is very consistent with the PL results of longer charge carrier lifetime and lower trap density for prolonged annealing time. Notably, current at both grains and grain boundaries is highly enhanced, which implies that both surface and bulk traps are significantly reduced by the thermally induced PbI_2 by longer annealing time.

Figure 7a shows the best performing 80 min annealed $FA_{0.9}Cs_{0.1}PbI_3$ PSK solar cell achieved by optimizing precursor solution. From the reverse scan, PCE of 20.36% (J_{SC}, 24.10 mA/cm^2; V_{OC}, 1.10 V; and FF, 0.768) is demonstrated. The integrated J_{SC} based on external quantum efficiency (EQE) spectrum is calculated to be 20.57 mA/cm^2. The relatively large discrepancy (~17%) between J_{SC}s measured using solar simulator and calculated from EQE is probably due to slow response of photocurrent and/or white light soaking effect as observed in previous report with similar device architecture (FTO/compact-TiO_2/$FA_{0.9}Cs_{0.1}PbI_3$/spiro-MeOTAD/Ag) along with contribution of capacitive current in $J-V$ curves. Steady-state Jsc and PCE under illumination can give more accurate and reliable values. The stabilized PCE is measured to be 18.84% under constant illumination and at bias voltage of 0.921 V (Figure 7b).

In conclusion, herein we investigated the correlation between defects in PSK layer and the current−voltage characteristics.

DOI: 10.1021/acs.nanolett.7b01211
Nano Lett. XXXX, XXX, XXX−XXX

The native defect density in PSK layer was controlled by thermally induced PbI_2 without significant change in morphology and crystallinity of the film. Strong correlation between the defect density and $J-V$ hysteresis was confirmed from device characterization and PL measurement, in which higher defect density was found to significantly contribute to the $J-V$ hysteresis and degradation of photovoltaic performance. Decoupling morphology and crystallinity factor, which can affect other possible factors for hysteresis, allow us to confirm direct correlation between native defect density in PSK layer and $J-V$ hysteresis phenomenon. Finally, stabilized PCE of 18.84% was demonstrated with the planar $FA_{0.9}Cs_{0.1}PbI_3$ PSK solar cell using optimized thermal annealing process.

■ ASSOCIATED CONTENT

Supporting Information

The Supporting Information is available free of charge on the ACS Publications website at DOI: 10.1021/acs.nanolett.7b01211.

Experimental methods, supplemental discussion, additional current density−voltage curves, energy dispersive X-ray spectroscopy (EDS) analysis (PDF)

■ AUTHOR INFORMATION

Corresponding Authors

*E-mail: yangy@ucla.edu. Phone: +1-310-825-4052.
*E-mail: npark@skku.edu. Phone: +82-31-290-7241.

ORCID

Yang Yang: 0000-0001-8833-7641
Nam-Gyu Park: 0000-0003-2368-6300

Author Contributions

J.-W.L and S.-G.K. contributed equally to this work. N.-G.P. and J.-W.L conceived experiments and prepared manuscript. J.-W.L., S.-G.K., and D.-K.L. prepared and characterized materials and devices. S.-H.B. and O.L. measured and analyzed c-AFM. Y.Y. prepared and revised manuscript. All authors discussed the results and commented on the manuscript.

Notes

The authors declare no competing financial interest.

■ ACKNOWLEDGMENTS

This work was supported by the National Research Foundation of Korea (NRF) Grants funded by the Ministry of Science, ICT & Future Planning (MSIP) of Korea under Contract Nos. NRF-2012M3A6A7054861 (Global Frontier R&D Program on Center for Multiscale Energy System), NRF-2015M1A2A2053004 (Climate Change Management Program), and NRF-2012M3A7B4049986 (Nano Material Technology Development Program). This work was also supported in part by NRF-2016M3D1A1027663 and NRF-2016M3D1A1027664 (Future Materials Discovery Program). Y.Y. acknowledges the financial support from Air Force Office of Scientific Research (AFOSR, Grant FA9550-15-1-0610) and Office of Naval Research (ONR, Grant N00014-04-1-0434).

■ REFERENCES

(1) Kojima, A.; Teshima, K.; Shirai, Y.; Miyasaka, T. *J. Am. Chem. Soc.* **2009**, *131*, 6050−6051.
(2) Im, J.-H.; Lee, C.-R.; Lee, J.-W.; Park, S.-W.; Park, N.-G. *Nanoscale* **2011**, *3*, 4088−4093.
(3) Kim, H.-S.; Lee, C.-R.; Im, J.-H.; Lee, K.-B.; Moehl, T.; Marchioro, A.; Moon, S.-J.; Humphry-Baker, R.; Yum, J.-H.; Moser, J. E.; Grätzel, M.; Park, N.-G. *Sci. Rep.* **2012**, *2*, 591.
(4) Lee, M. M.; Teuscher, J.; Miyasaka, T.; Murakami, T. N.; Snaith, H. J. *Science* **2012**, *338*, 643−647.
(5) Best Research-Cell Efficiencies. http://www.nrel.gov/ncpv/images/efficiency_chart.jpg (accessed March 21, 2017).
(6) Burschka, J.; Pellet, N.; Moon, S.-J.; Humphry-Baker, R.; Gao, P.; Nazeeruddin, M. K.; Grätzel, M. *Nature* **2013**, *499*, 316−319.
(7) Lee, J.-W.; Seol, D.-J.; Cho, A.-N.; Park, N.-G. *Adv. Mater.* **2014**, *26*, 4991−4998.
(8) Lee, J.-W.; Kim, H.-S.; Park, N.-G. *Acc. Chem. Res.* **2016**, *49*, 311−319.
(9) Jeon, N. J.; Noh, J. H.; Kim, Y. C.; Yang, W. S.; Ryu, S.; Seok, S. I. *Nat. Mater.* **2014**, *13*, 897−903.
(10) Chen, Q.; Zhou, H.; Hong, Z.; Luo, S.; Duan, H.-S.; Wang, H.-H.; Liu, Y.; Li, G.; Yang, Y. *J. Am. Chem. Soc.* **2014**, *136*, 622−625.
(11) Liu, M.; Johnston, M. B.; Snaith, H. J. *Nature* **2013**, *501*, 395−398.
(12) Xing, G.; Mathews, N.; Sun, S.; Lim, S. S.; Lam, Y. M.; Grätzel, M.; Mhaisalkar, S.; Sum, T. C. *Science* **2013**, *342*, 344−347.
(13) Stranks, S. D.; Eperon, G. E.; Grancini, G.; Menelaou, C.; Alcocer, M. J.; Leijtens, T.; Herz, L. M.; Petrozza, A.; Snaith, H. J. *Science* **2013**, *342*, 341−344.
(14) Dong, Q.; Fang, Y.; Shao, Y.; Mulligan, P.; Qiu, J.; Cao, L.; Huang, J. *Science* **2015**, *347*, 967−970.
(15) Yin, W.-J.; Shi, T.; Yan, Y. *Appl. Phys. Lett.* **2014**, *104*, 063903.
(16) D'Innocenzo, V.; Grancini, G.; Alcocer, M. J.; Kandada, A. R. S.; Stranks, S. D.; Lee, M. M.; Lanzani, G.; Snaith, H. J.; Petrozza, A. *Nat. Commun.* **2014**, *5*, 3586.
(17) Kim, H.-S.; Kim, S. K.; Kim, B. J.; Shin, K.-S.; Gupta, M. K.; Jung, H. S.; Kim, S.-W.; Park, N.-G. *J. Phys. Chem. Lett.* **2015**, *6*, 1729−1735.
(18) Xiao, Z.; Yuan, Y.; Shao, Y.; Wang, Q.; Dong, Q.; Bi, C.; Sharma, P.; Gruverman, A.; Huang, J. *Nat. Mater.* **2014**, *14*, 193−198.
(19) Sanchez, R. S.; Gonzalez-Pedro, V.; Lee, J.-W.; Park, N.-G.; Kang, Y. S.; Mora-Sero, I.; Bisquert, J. *J. Phys. Chem. Lett.* **2014**, *5*, 2357−2363.
(20) Leguy, A. M.; Frost, J. M.; McMahon, A. P.; Sakai, V. G.; Kockelmann, W.; Law, C.; Li, X.; Foglia, F.; Walsh, A.; O'regan, B. C.; Nelson, J.; Carbral, J. T.; Barnes, P. R. F. *Nat. Commun.* **2015**, *6*, 7124.
(21) Snaith, H. J.; Abate, A.; Ball, J. M.; Eperon, G. E.; Leijtens, T.; Noel, N. K.; Stranks, S. D.; Wang, J. T.-W.; Wojciechowski, K.; Zhang, W. *J. Phys. Chem. Lett.* **2014**, *5*, 1511−1515.
(22) Kim, H.-S.; Park, N.-G. *J. Phys. Chem. Lett.* **2014**, *5*, 2927−2934.
(23) Almora, O.; Zarazua, I.; Mas-Marza, E.; Mora-Sero, I.; Bisquert, J.; Garcia-Belmonte, G. *J. Phys. Chem. Lett.* **2015**, *6*, 1645−1652.
(24) Kim, H.-S.; Jang, I.-H.; Ahn, N.; Choi, M.; Guerrero, A.; Bisquert, J.; Park, N.-G. *J. Phys. Chem. Lett.* **2015**, *6*, 4633−4639.
(25) Azpiroz, J. M.; Mosconi, E.; Bisquert, J.; De Angelis, F. *Energy Environ. Sci.* **2015**, *8*, 2118−2127.
(26) Frost, J. M.; Butler, K. T.; Walsh, A. *APL Mater.* **2014**, *2*, 081506.
(27) Yu, H.; Lu, H.; Xie, F.; Zhou, S.; Zhao, N. *Adv. Funct. Mater.* **2016**, *26*, 1411−1419.
(28) Lee, J.-W.; Kim, D. H.; Kim, H.-S.; Seo, S. W.; Cho, S. M.; Park, N.-G. *Adv. Energy Mater.* **2015**, *5*, 1501310.
(29) Ko, H.-S.; Lee, J.-W.; Park, N.-G. *J. Mater. Chem. A* **2015**, *3*, 8808−8815.
(30) Wang, Q.; Chen, B.; Liu, Y.; Deng, Y.; Bai, Y.; Dong, Q.; Huang, J. *Energy Environ. Sci.* **2017**, *10*, 516−522.
(31) de Quilettes, D. W.; Vorpahl, S. M.; Stranks, S. D.; Nagaoka, H.; Eperon, G. E.; Ziffer, M. E.; Snaith, H. J.; Ginger, D. S. *Science* **2015**, *348*, 683−686.
(32) Son, D.-Y.; Lee, J.-W.; Choi, Y. J.; Jang, I.-H.; Lee, S.; Yoo, P. J.; Shin, H.; Ahn, N.; Choi, M.; Kim, D.; Park, N.-G. *Nat. Energy* **2016**, *1*, 16081.
(33) Wen, X.; Feng, Y.; Huang, S.; Huang, F.; Cheng, Y.-B.; Green, M.; Ho-Baillie, A. *J. Mater. Chem. C* **2016**, *4*, 793−800.

DOI: 10.1021/acs.nanolett.7b01211
Nano Lett. XXXX, XXX, XXX−XXX

(34) Yin, W. J.; Shi, T.; Yan, Y. *Adv. Mater.* **2014**, *26*, 4653−4658.
(35) Roldan-Carmona, C.; Gratia, P.; Zimmermann, I.; Grancini, G.; Gao, P.; Grätzel, M.; Nazeeruddin, M. K. *Energy Environ. Sci.* **2015**, *8*, 3550−3556.
(36) Kim, Y. C.; Jeon, N. J.; Noh, J. H.; Yang, W. S.; Seo, J.; Yun, J. S.; Ho-Baillie, A.; Huang, S.; Green, A. M.; Seidel, J.; Ahn, T. K.; Seok, S. I. *Adv. Energy Mater.* **2016**, *6*, 1502104.
(37) Chen, Q.; Zhou, H.; Song, T.-B.; Luo, S.; Hong, Z.; Duan, H.-S.; Dou, L.; Liu, Y.; Yang, Y. *Nano Lett.* **2014**, *14*, 4158−4163.
(38) Supasai, T.; Rujisamphan, N.; Ulich, K.; Chemseddine, A.; Dittrich, Th. *Appl. Phys. Lett.* **2013**, *103*, 183906.
(39) Wang, L.; McCleese, C.; Kovalsky, A.; Zhao, Y.; Burda, C. *J. Am. Chem. Soc.* **2014**, *136*, 12205−12208.
(40) Shih, M.-C.; Li, S.-S.; Hsieh, C.-H.; Wang, Y.-C.; Yang, H.-D.; Chiu, Y.-P.; Chang, C.-S.; Chen, C.-W. *Nano Lett.* **2017**, *17*, 1154−1160.
(41) Yin, W.-J.; Chen, H.; Shi, T.; Wei, S.-H.; Yan, Y. *Adv. Electron. Mater.* **2015**, *1*, 1500044.
(42) Heo, J. H.; Han, H. J.; Kim, D.; Ahn, T. K.; Im, S. H. *Energy Environ. Sci.* **2015**, *8*, 1602−1608.
(43) Shao, Y.; Fang, Y.; Li, T.; Wang, Q.; Dong, Q.; Deng, Y.; Yuan, Y.; Wei, H.; Wang, M.; Gruverman, A.; Shielda, J.; Huang, J. *Energy Environ. Sci.* **2016**, *9*, 1752−1759.
(44) Yuan, Y.; Huang, J. *Acc. Chem. Res.* **2016**, *49*, 286−293.

DOI: 10.1021/acs.nanolett.7b01211
Nano Lett. XXXX, XXX, XXX−XXX